Density-dependent Hartree-Fock description of nuclei in the rare earth and nickel regions*

J. W. Negele†
Laboratory for Nuclear Science and Department of Physics, Massachusetts Institute of Technology, Cambridge, Massachusetts 02139

G. Rinker‡
Physics Division, Los Alamos Scientific Laboratory, Los Alamos, New Mexico 87545

(Received 10 June 1976; revised manuscript received 22 November 1976)

Motivated by recent high-resolution muonic x-ray and electron scattering experiments, the mean field approximation with a realistic effective interaction has been applied in the rare-earth and nickel regions. For rotational rare-earth nuclei, the approximation of a single axially symmetric deformed intrinsic state yields quantitative agreement with the experimental binding energies, deformations, elastic electron scattering, and inelastic electron scattering to 2^+ states. Discrepancies in transitions to 4^+ and 6^+ states may indicate the limits of validity of the simple deformed intrinsic state approximation. The recent radius measurements in Fe, Ni, and Zn isotopes have made it possible to test the degree to which the systematics of polarization of the charge distributions of nonspherical nuclei may be understood through the mean-field approximation. Although certain significant qualitative features have been understood, it is shown that the deformations of nuclei in this region are insufficiently defined to validate approximation by a single intrinsic wave function.

[NUCLEAR STRUCTURE ^{148,150}Nd, ^{152,154}Sm, ^{156}Gd, ^{166}Er, ^{176}Yb, ^{238}U, ^{252}Cf, ^{54,56,58}Fe, ^{58,60,62,64}Ni, ^{64,66,68,70}Zn. Density-dependent Hartree-Fock predictions of energies and densities, comparison with electron scattering and muonic x-ray experimental results.]

I. INTRODUCTION

The density-dependent Hartree-Fock (DDHF) theory has been extremely successful in providing a microscopic understanding of the energies and charge density distributions of spherical nuclei.[1] The two essential features of this theory for our present purposes are the mean-field approximation, in which a single determinantal wave function is obtained by solving for single-particle wave functions in the mean field generated by the other particles, and the fact that, aside from minor adjustments to obtain proper saturation, the interaction is obtained from a reaction matrix calculated from a realistic potential.

The simplicity of the mean-field approximation distinguishes DDHF from the more rigorous many-body treatments of light nuclei involving the solution of three-body equations.[2] Fortunately, it appears that the essential physics from the three-body terms may be included in an appropriate definition of the particle potential in the reaction matrix,[3] or equivalently, in the adjustment of the two-body effective interaction. Hence, DDHF enables one to extend an essentially microscopic approach to regimes of heavy and deformed nuclei where rigorous microscopic calculations are presently unfeasible.

The fact that the effective interaction is calculated from a realistic interaction distinguishes the present theory from those which utilize purely phenomenological interactions. Although there is no question that numerous varieties of phenomenological interactions can be adjusted to reproduce energy systematics as well as reasonable density distributions,[4] we have sought in this work to be guided as fully as possible by our present knowledge of the nuclear interaction and to introduce no additional parameters for nonspherical nuclei. Given the success of the interaction in spherical nuclei throughout the Periodic Table, we believe that any discrepancies arising in the rare-earth or nickel regions should be attributed to other physical origins, and not absorbed into new parameters in the effective interaction.

In considering the application of DDHF to other than spherical closed-shell nuclei, it is useful to recall the semiclassical features inherent in the mean-field or Hartree-Fock (HF) approximation. Already in the case of spherical nuclei, the c.m. wave function is treated semiclassically. In contrast to the true quantal factorized wave function comprised of a relative $N-1$-body wave function multiplying a delocalized c.m. wave function, the determinantal wave function approximately localizes the position of the c.m. At best, then, the determinant represents a wave packet of states, prepared to approximately localize the position of the nucleus. In order to calculate an intrinsic density distribution for comparison

with electromagnetic measurements, the effect of the c.m. zero-point motion, or the extent of the c.m. wave packet, must be removed from the wave function by some appropriate projection prescription. Since the c.m. motion is not quantized, and the wave function is not rigorously factorizable, it is evident that any such projection is necessarily ambiguous and nonunique.

An analogous situation arises for well-deformed rotational nuclei. When the mean-field approximation yields an axially symmetric deformed determinantal wave function, this intrinsic state must be understood as a wave packet comprised of different angular momentum states superimposed in such a way as to localize the orientation of the nucleus. As before, one may attempt to project individual angular momentum states from this wave packet, but ambiguities and questions of uniqueness necessarily arise.

Yet another complication occurs if the nucleus is very soft with respect to shape deformations. If the total energy with a trial wave function changes only very slowly as the deformation of the trial function is varied, then the zero-point fluctuations in this collective degree of freedom will sample a wide range of different, but nearly degenerate, configurations. Thus, approximating the state by a single determinant may leave out essential components of the wave function.

The goal of this work, then, is to investigate how serious these limitations are in the application of the mean-field approximation to nuclei in the rare-earth and nickel regions. For the well-deformed rare-earth nuclei, the primary issue will be the validity of extracting different angular momentum states from a single deformed intrinsic wave function. In the nickel region the emphasis will be on the polarization, or static response, of the protons generated by the addition or removal of nucleons. Whereas in spherical nuclei, polarization is quite well explained by DDHF in terms of the spherically symmetric dilation of the core proton distribution, the question arises as to whether the changes in shapes and deformation between isotopes and isotones in soft, nonspherical nuclei are adequately described by the mean-field approximation.

The choice of nuclei investigated in this work is motivated by recent leptonic experiments. The rare earths were selected because of old electron scattering data[5] from the National Bureau of Standards (NBS) and especially because of the new high-resolution elastic and inelastic measurements of transitions up to 6^+ states on ^{150}Nd, ^{156}Gd, ^{166}Er, and ^{176}Yb at Bates.[6] Calculations in the nickel region were motivated by the combination of extensive muonic x-ray measurements on ^{54,56,58}Fe, ^{56,60,62,64}Ni, and ^{64,66,68,70}Zn at Los Alamos[7] and comparison elastic electron scattering measurements at Mainz.[8] The additional calculation of the two actinides ^{238}U and ^{252}Cf was motivated by the planned ^{238}U experiment at Bates and the desire to check radii, binding energies, and quadrupole moments at the extreme end of the Periodic Table.

II. DDHF CALCULATIONS FOR AXIALLY SYMMETRIC DEFORMED NUCLEI

A. Computational method

The deformed DDHF calculations have been performed using the density matrix expansion (DME) effective Hamiltonian of Ref. 11 and the deformed oscillator expansion techniques developed in Refs. 9 and 10 for Skyrme forces. By use of the DME it was shown that an energy density functional of the same simplicity as that obtained with the Skyrme force could be derived from a realistic two-body effective interaction. Thus, it is straightforward to utilize the technology of Ref. 10 by simply replacing the potential $U_\eta(r)$ [Eq. (2.2) of Ref. 10] and $1/m^*(r)$ [Eq. (2.2b)] expressed in terms of the density, kinetic energy density, and Skyrme parameters by Eqs. (5.1) and (5.2) of Ref. 11, which involve only the density, kinetic energy density, and numerical coefficients determined uniquely by the two-body effective interaction. All parameters of the effective interaction as used in this work are presented in the text and Table I of Ref. 11.

The replacement of the Skyrme parameters by the DME functional in Vautherin's code was implemented by Brack,[12] and served as a starting point for the present calculation.

B. Convergence

To obtain adequate numerical convergence, two changes relative to Ref. 10 were introduced. The upper limit N_0 on the total number of oscillator quanta was increased to 16, where N_0 is defined such that $\omega_z(n_z+\frac{1}{2})+\omega_\perp(n_\perp+1)\leq(\omega_\perp^2\omega_z)^{1/3}(N_0+2)$ where n and ω denote the number of oscillator quanta and oscillator frequencies in the z direction and perpendicular to the z direction. Computation of oscillator space matrix elements of the HF potential in coordinate space requires numerical integrations over $\eta=r^2$ and z of products of single-particle wave functions times powers of the density and kinetic energy density. Since the wave functions are comprised of exponentials in z^2 and η multiplied by polynomials in z and in η, finite order Gauss-Hermite and Gauss-Laguerre integrations could in principle yield exact results.

However, even for the Skyrme potential, more than N_0 points would be required, since in addition to the two oscillator wave functions appearing in the matrix elements, U_n contains ρ^2, introducing very high degree polynomials. For the DME functional, even higher powers of the density arise, so it is clear that one cannot do the numerical integrals exactly, but must rather check numerically that the accuracy is commensurate with that of the rest of the calculation. For this reason, the number of Gauss-Hermite and Gauss-Laguerre integration points, denoted K, was made adjustable up to $K=16$. A numerical study of convergence with respect to N_0 and K is presented in Appendix A.

C. Pairing

As in Refs. 9 and 10, a constant gap Δ taken from experimental mass differences is assumed and the functional

$$\langle H\rangle - \Delta \sum_i v_i(1-v_i^2)^{1/2} \tag{1}$$

is minimized subject to the constraint $\sum_i v_i^2 = N$ where v_i is the occupation probability of the ith orbital. The actual energy is given by

$$E = \langle H\rangle - \tfrac{1}{2}\Delta \sum_i v_i(1-v_i^2)^{1/2} \tag{2}$$

and the approximation is equivalent to postulating constant state-independent $J=0$ $T=1$ matrix elements of the two-body potential of magnitude $2\Delta/\sum_i v_i(1-v_i^2)^{1/2}$.

This treatment of pairing suffers from several serious limitations. Actual calculation of $J=0$ $T=1$ matrix elements[13] shows significant state dependence. Furthermore, these matrix elements clearly should depend upon the deformation, yielding a deformation-dependent gap. In contrast to a full Hartree-Fock-Bogoliubov calculation, variation of Eq. (1) which double counts the pairing energy relative to Eq. (2) does not minimize the total energy. Thus, if pairing effects were significant, one would have no assurance that the proper deformation minimum had been attained.

However, in this present work, we do not believe that the crude treatment of pairing should have a significant effect for cases in which the theory otherwise makes sense. The primary motivation for including pairing in the first place is simply the convenience with which it handles level crossings. For cases in which the energy of deformation surface has deep minima, the small shift in the position of the minimum by inaccuracy in the pairing should be negligible. For shallow minima, as we shall subsequently argue, the large zero-point fluctuations invalidate the mean-field approximation in any event, so errors in the treatment of pairing are irrelevant. As a final argument against a more sophisticated treatment of pairing, it seems likely that if the residual interaction effects included in the simple pairing approximation are dominating the structure, then other configurations and other matrix elements beside the $J=0$ $T=1$ elements retained in the pairing theory will also be significant.

D. External constraints

Since we are concerned with static deformed DDHF determinantal wave functions, there is no necessity for introducing constraints on the shape. Simply choosing a representative variety of initial wave function and iterating to self-consistency suffices to locate the stable self-consistent solutions. Nevertheless, the quadratic constraint of Ref. 9 on the mass quadrupole moment was utilized in this work for two reasons. The first was simply as a technical convenience to facilitate the location of enery minima by first mapping out the energy of deformation vs quadrupole moment curve. The second, and physically motivated reason, was to use the energy of deformation curves to assess the validity of the description in terms of one single intrinsic state of a specific deformation.

Formally, the introduction of a term in the mean field proportional to Q yields pathologically large attractive potentials far from the nucleus, either in the x-y plane or along the z axis. In practice, even in the large oscillator bases employed in this work, this distant unphysical potential never affects the calculation because the oscillator basis functions do not penetrate significantly into this region. If a problem were ever to arise, it could be resolved by introducing any sensible cutoff into the definition of the constraining field.

E. Transition densities

For subsequent reference and discussion, it will be useful to establish formulas for transition densities and multipole moments. Ideally, we would like to calculate the density between eigenstates of angular momentum l and angular momentum zero. Restricting ourselves to a single determinantal wave function for each state, the best approximation would be to project out the desired angular momentum component and then vary the single-particle wave functions. In this work, however, the variation is performed before projection, yielding a single intrinsic state out of which individual angular momentum states must be projected.

For an axially symmetric $K=0$ intrinsic state, the matrix element of the density operator between projected states of angular momentum l and angular momentum 0 is

$$\langle l|\hat{\rho}|0\rangle = \frac{\langle\psi_{\rm HF}|\hat{P}^{l}_{00}\hat{\rho}\hat{P}^{0}_{00}|\psi_{\rm HF}\rangle}{\|\hat{P}^{l}_{00}|\psi_{\rm HF}\rangle\|\|\hat{P}^{0}_{00}|\psi_{\rm HF}\rangle\|} = \frac{N}{r^2}\int d\cos\beta\langle\psi_{\rm HF}|\sum_i \delta(r-x_i)Y^*_{l0}(\Omega_i)e^{-\beta J_y}|\psi_{\rm HF}\rangle, \tag{3}$$

where $\hat{P}^{L}_{MK}$ is a projection operator and N is an overall normalization factor.

Using standard many-body techniques,[14]

$$\langle\psi|\hat{O}e^{-i\beta J_y}|\psi\rangle = \exp(\langle\psi|e^{-i\beta J_y}|\psi\rangle_c)\,\langle\psi|\hat{O}^{-i\beta J_y}|\psi\rangle_L \approx \exp(-\tfrac{1}{2}\beta^2\langle\psi|J_y{}^2|\psi\rangle)\langle\psi|\hat{O}e^{-i\beta J_y}|\psi\rangle_L . \tag{4}$$

Thus, in the limit of large $\langle J_y^2\rangle$, the β integration is restricted to an arbitrarily narrow range, and the matrix element is approximately given by

$$\langle l0|\hat{\rho}|00\rangle \approx \langle\psi_{\rm HF}|\sum_i \delta(r-x_i)Y^*_{l0}(\Omega_i)|\psi_{\rm HF}\rangle = \int d\Omega\,\rho_{\rm HF}(r,\theta)Y_{l0}(\Omega). \tag{5}$$

In this limit, the transition density is just given by the Legendre expansion of the intrinsic density distribution. To adhere to the definitions in Ref. 10, which differ from those of Ref. 5 by the factor $[(2l+1)/4\pi]^{1/2}$, we shall define the transition densities by

$$\rho_l \equiv \left(\frac{2l+1}{4\pi}\right)^{1/2}\int d\Omega\,\rho_{\rm HF}(r,\theta)Y^*_{l0}(\Omega) = (2l+1)\int_0^{\pi/2}\rho(r,\theta)P_l(\theta)\sin\theta\,d\theta \tag{6}$$

and the multipole moments by

$$Q_l = \frac{8\pi}{2l+1}\int_0^\infty \rho_l(r)r^{2+l}\,dr. \tag{7}$$

With these conventions, the reduced transition probabilities are given by

$$[B(El)]^{1/2} = \frac{1}{2}\left(\frac{2l+1}{4\pi}\right)^{1/2}Q_l. \tag{8}$$

By Legendre expansion of the proton form factor,[10] the transition charge densities may be obtained from proton densities by the relation

$$\rho_l^{\rm ch}(r) = \int_0^\infty r'^2\,dr' I_l(r,r')\rho_l^p(r'), \tag{9}$$

where $I_l(r,r') = 2\pi\int_{-1}^{1}dx f[(r^2+r'^2-2rr'x)^{1/2}]P_l(x)$ and f is the proton form factor. For an exponential form factor, values of I_l may be generated straightforwardly by writing recursion relations for the quantities

$$\hat{I}_l(r,r') = \int_{-1}^{1}dx\,P_l(x)e^{-\alpha z}$$

and

$$\hat{J}_l(r,r') = \int_{-1}^{1}dx\,P_l(x)ze^{-\alpha z},$$

where

$$z = (r^2+r'^2-2rr'x)^{1/2} \tag{10}$$

provided the instability of upward recursion for small arguments is recognized. Multipole moments for the charge density are identical to those of the proton density, since the proton charge distribution is isotropic.

III. RARE-EARTH NUCLEI

The results of calculations for selected rare-earth (and actinide) nuclei are summarized in Figs. 1–5 and Table I.

A. Binding energies

The systematic agreement between theoretical and experimental binding energies shown in column 7 of Table I is comparable to that obtained for spherical nuclei in Ref. 11. Comparison with experiment is somewhat complicated by the fact that starting energy corrections[11] were not explicitly calculated in this work, and the parameters as tabulated in Ref. 11 were defined such that these corrections are approximately cancelled in ^{208}Pb. Thus, a correction Δ is estimated according to

$$\frac{\Delta}{A} = aA^{-1/3} + b \tag{11}$$

based on the fact[15] that the starting energy correction is essentially a surface term and that in Ref. 11 it was roughly compensated by a volume term. Fitting a and b from the known discrepancies in ^{90}Zr and ^{208}Pb leads to the corrected energies tabulated in column 8. Whereas it is gratifying that the discrepancies are reduced to less than 0.05 MeV per particle, the correction Δ is at best an order of magnitude estimate. Furthermore, we have not included the correction of from 0.02 to 0.04 MeV per particle arising from the fact that the intrinsic state is a superposition of different angular momentum states.[16] Thus, at the present level of accuracy of the theory, the binding energies appear quite satisfactory.

B. Binding energy as a function of Q_0

Calculations with a quadratic constraint on the value of the mass quadrupole moment Q_0 yield the

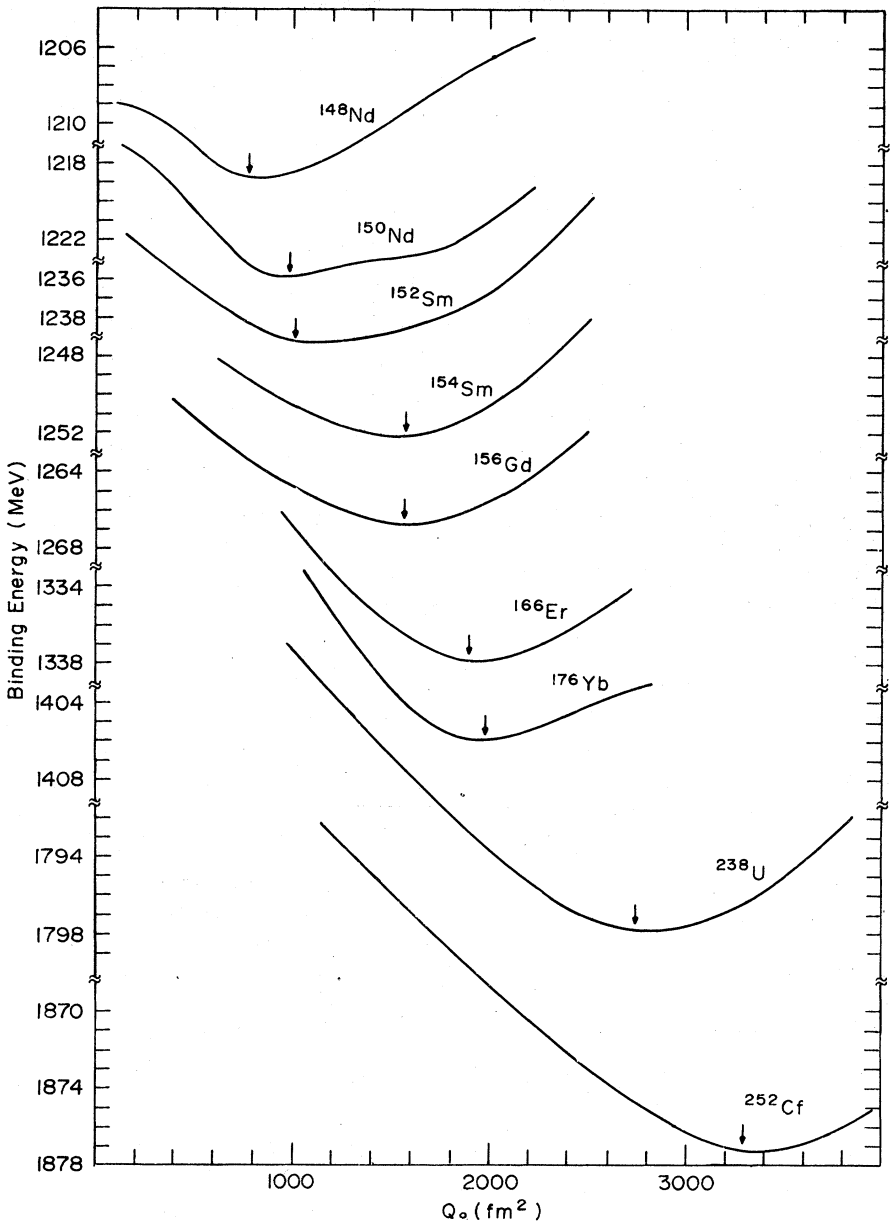

FIG. 1. Energy of deformation curves vs mass quadrupole moment for selected rare earths and actinides.

energy of deformation curves shown in Fig. 1. The binding energy was calculated according to Eq. (2) and the positions of the unconstrained self-consistent results are indicated by the arrows. One observes a distinction between the rather shallow minima, small deformations, and low spherical barriers of ^{148}Nd, ^{150}Nd, and ^{152}Sm, and the narrower minima, large deformations, and high spherical barriers of the remaining nuclei. A similar progression has been reported by Decharge, Girod, and Gogny for the samarium isotopes.[17] It is significant that the first three nuclei, for which the approximation of a single deformed intrinsic state is suspect on the basis of the theoretical deformation energy curves, coincide precisely with the nuclei which experimentally do not have good rotational spectra. As criteria for good rotational spectra, experimental energy ratios $3E_4^+/10E_2^+$ and $E_8^+/12E_2^+$, both of which should be unity if energies were proportional to $I(I+1)$, are tabulated in the last two columns of Table I.

For the first three nuclei in Table I, the discrepancy in the 4^+ energy is at least 10% whereas for all others it is less than 3%. Furthermore,

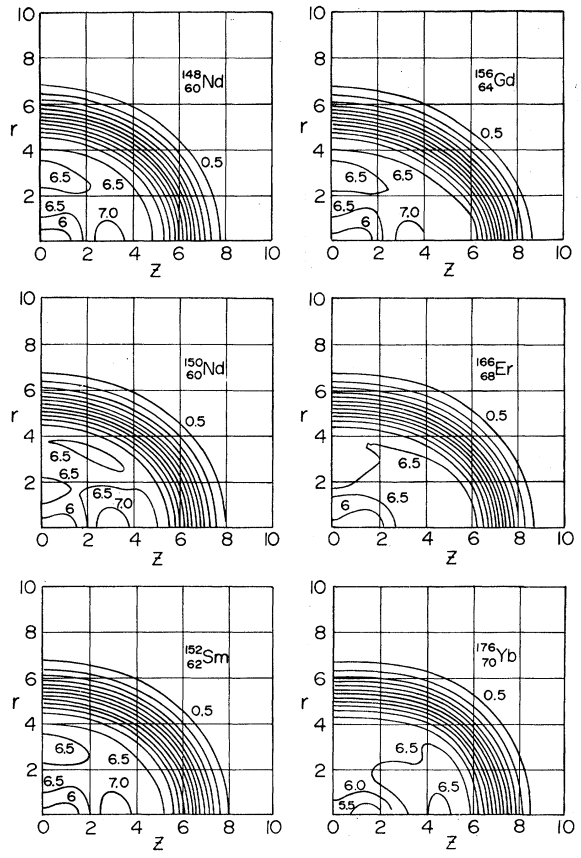

FIG. 2. Contour plots of proton density distributions. The density contours are in increments of 0.005 fm^{-3}, the labels denote the density multiplied by 100, and r and z are in fm.

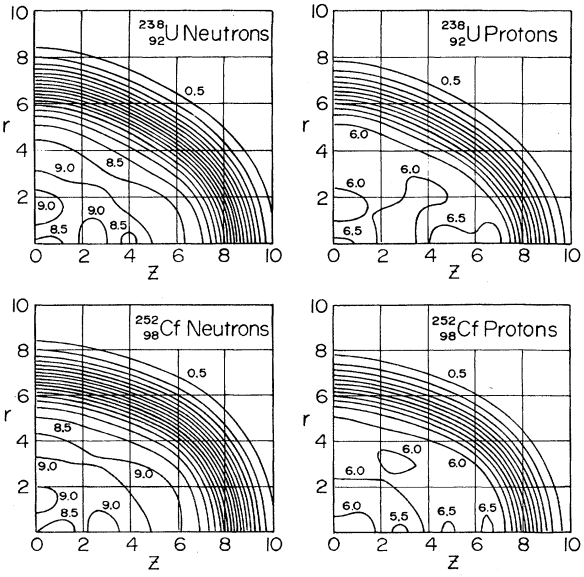

FIG. 3. Proton and neutron density contours for actinides. Scales are as in Fig. 2.

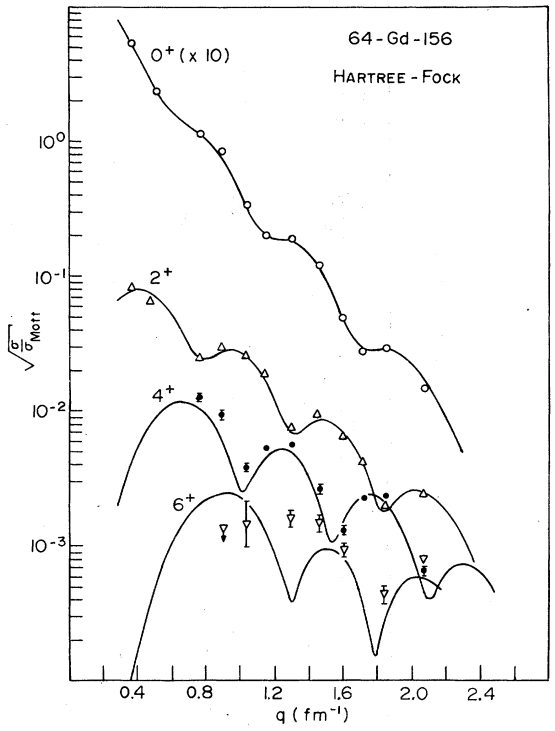

FIG. 4. Elastic and inelastic DWBA form factors for ^{156}Gd. The notation J^+ denotes a transition from $0^+ \rightarrow J^+$, the solid lines are the theoretical prediction, and the error bars denote the experimental results of Ref. 6.

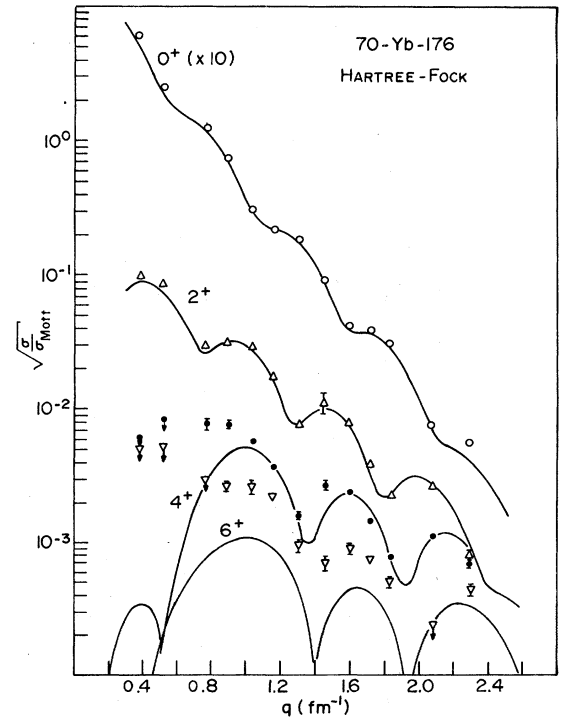

FIG. 5. Elastic and inelastic DWBA form factors for ^{176}Yb, with the same notation as Fig. 6.

TABLE I. Moments, binding energies, and ratios of experimental excitation energies for rare-earth and actinide nuclei as described in the text. The top entries for each nucleus denote theoretical predictions.

	Q_2^P (fm^2)	Q_4^P (fm^4)	r^c (fm)	Q_2^N (fm^2)	Q_4^N (fm^4)	r^N (fm)	$\frac{BE_{expt} - BE_{th}}{A}$ (MeV)	$\frac{BE_{expt} - BE_{th} - \Delta}{A}$ (MeV)	$\frac{3}{10}\frac{E_4^+}{E_2^+}$	$\frac{1}{12}\frac{E_8^+}{E_2^+}$
^{148}Nd	312	1433	4.990	457	3855	5.126	0.084	−0.050		
			5.002[a]						0.790	
^{150}Nd	388	2258	5.013	589	4929	5.163	0.090	−0.040		
	515(10)[b]		5.015(37)[a]						0.902	
	515(5)[c]		5.048[b]							
^{152}Sm	413	2160	5.053	592	4515	5.175	0.091	−0.035		
	578(10)[b]	8700(400)[d]	5.092						0.903	
	593(3)[c]		5.090							
^{154}Sm	641	9779	5.1140	923	15720	5.2423	0.095	−0.030		
	760[b]	11100(200)[d]	5.126						0.977	0.966
	665(7)[c]									
^{156}Gd	654	8500	5.146	906	13520	5.249	0.095	−0.022		
	691(6)[c]								0.972	0.899
^{166}Er	778	6586	5.262	1108	10730	5.365	0.083	−0.014		
	758(6)[c]	7200[d]	5.238[d]						0.987	0.941
^{176}Yb	791	1358	5.334	1183	1757	5.467	0.090	+0.014		
	765(22)[b]	2270[d]	5.32[b]						0.976	0.964
	732(8)[c]									
^{238}U	1042	23900	5.844	1700	38410	6.018	0.006	0.015		
	1130(20)[b]	25900[d]	5.843[a]						0.993	0.975
	1130(8)[c]									
^{252}Cf	1285	17930	5.977	1990	23830	6.132	0.003	0.028		
	1292[e]									

[a] Reference 17.
[b] Reference 18.
[c] Reference 19.
[d] Reference 5.
[e] Reference 20.

8^+ states are not observed for the first three, whereas they are seen to be quite consistent with the rotational model for all others. It is particularly interesting to see the sharp distinction predicted theoretically between ^{152}Sm and ^{154}Sm, which is also consistent with the observed spectra. The mechansim for this sharp transition is quite evident from the theoretical single-particle energy levels. Near the last occupied neutron state in ^{152}Sm lie two unoccupied levels with Nilsson quantum numbers [660] and [651] arising from the $\frac{1}{2}^+$ and $\frac{3}{2}^+$ components of the $i_{13/2}$ shell. The energies of these two prolate levels decrease strongly with increasing deformation, and in the present calculation, the self-consistent effect of adding two neutrons to ^{152}Sm is such that a small increase in deformation changes the level ordering, and the occupation of both these extremely prolate states then increases the deformation by more than 50%.

C. Moments of charge densities

Calculated rms charge radii, corrected for the proton form factor, are compared with values deduced from experiments[5,18,19] in column 3 of Table I. Aside from ^{150}Nd and ^{152}Sm, the radii agree to within 0.02 fm, which is the level at which one would, in any case, suspect the accuracy of the extraction of the rms radii from experiment.[4] Consistent with our previous arguments concerning the deformation curves, we attribute the discrepancies in ^{150}Nd and ^{152}Sm to the breakdown of the approximation of a single intrinsic state of fixed deformation for these nuclei.

Proton quadrupole and hexadecapole moments defined according to Eq. (7) are tabulated in the first two columns of Table I and compared, where possible, with experiment.[5,19-21] With the exception of the first three nuclei, the systematics of the increase of the quadrupole moments with increasing A are reproduced in detail by the theory. Even more dramatic is the agreement in all but the first three nuclei of the Q_4 moments, which decrease strongly with increasing A in the rare earths and then increase in the actinides.

The behavior of the hexadecapole moment in the rare earths was emphasized in Ref. 5, where the shape change from Sm to Yb was visually noticeable on contour plots reconstructed from a Legendre expansion of the density determined from electron scattering. The same systematics predicted theoretically are evident from the proton density contour plots presented in Fig. 2. It is particularly easy to compare ^{156}Gd with ^{176}Yb, since the 0.5 and 1.0 contours intersect the r and z axes at essentially the same points, whereas along the diagonal $r = z$ they clearly differ. Another feature emphasized in Ref. 5, the kidney shaped maxima concentrated at the poles of ^{166}Er and ^{176}Yb, also appears in Fig. 2, where the 6.5 contours enclose similar kidney shaped regions in these nuclei. In addition to the inelastic electron scattering data which provide such direct spatial resolution, there exists considerable information relevant to hexadecapole deformation from Coulomb excitation, (α, α'), and (p, p') scattering. These data are generally analyzed in terms of β_4 values which must be deduced from an equivalent uniform density distribution, and an excellent summary of rare-earth data is presented in Fig. 1 of Ref. 16.

Contour plots for neutron and proton densities in the two actinide nuclei are shown in Fig. 3. Even more conspicuously than in the rare earths, in ^{238}U there is a relative depletion of density 45° away from the z axis and a relative accumulation along the r and z axes, giving rise to very large hexadecapole moments. Progressing to higher A in the actinides, just as in the rare earths, appears to diminish the hexadecapole moment, with ^{252}Cf displaying a significantly smaller hexadecapole deformation than ^{238}U.

D. Electron scattering

Elastic and inelastic electron scattering will be addressed at length in a subsequent article,[6] so we will restrict our present discussion to several salient points. Figures 4 and 5 compare distorted wave Born approximation (DWBA) calculations based on the transition densities given in Eq. (9) with experimental data from ^{156}Gd and ^{176}Yb. Results for ^{166}Er are qualitatively similar whereas, as expected from our discussion of the ^{150}Nd deformation curve, all inelastic cross sections predicted for Nd are in serious disagreement with experiment.

The quality of agreement of elastic form factors in Figs. 4 and 5 is comparable to that obtained throughout the Periodic Table in spherical nuclei with the same interaction.[1] The agreement for the $0^+ \rightarrow 2^+$ transitions is also quite good, not only in overall normalization but also in the detailed diffraction structure. In contrast, the $0^+ \rightarrow 4^+$ form factors are somewhat in error in magnitude although reasonably accurate in shape. Notice however, both theoretically and experimentally, the $0^+ \rightarrow 4^+$ transition density is significantly different in these two nuclei. The magnitude of the 4^+ relative to the 2^+ form factor is considerably larger in Gd, consistent with the larger Q_4 and resulting $B(E4)$. In addition, the phasing of oscillations in the 4^+ and 2^+ form factors is completely different in Gd and Yb, and to the extent to which

theory reproduces this phasing, the densities displayed in Fig. 2 are reproducing detailed spatial differences in density distributions. Finally we note that the $0^+ \rightarrow 6^+$ transitions are reproduced quite poorly. Although we are not aware of definitive calculations of dispersion corrections for these nuclei, we do not believe at present that such corrections account for the observed discrepancies.

E. Conclusions

From the preceding results, we conclude that for the well-deformed rotational nuclei the mean-field approximation with a single deformed intrinsic state is quite satisfactory, yielding gross properties as accurately as in spherical nuclei. The salient discrepancies in the rare-earth region include the gross properties of ^{148}Nd, ^{150}Nd, and ^{152}Sm and the details of transition densities to 4^+ and 6^+ rotational states. It is essential to the understanding of the underlying physics that the physical origins of these discrepancies be fully understood.

One conceivable explanation of both discrepancies would be to attribute them to the effective interaction, and thus seek some improved phenomenological interaction which fits more observables. From our experience in observing the sensitivity of equilibrium deformations in shallow minima and of the 4^+ and 6^+ transition densities to minor changes in interaction parameters, pairing strengths, and departures from self-consistency, it is also plausible that these discrepancies could be doctored by deliberately adjusting the force.

Our present inclination, however, is that it would be a mistake to try to resolve either of these discrepancies by changing the force. The fact that the deformation energy curves change abruptly between ^{152}Sm and ^{154}Sm, where the onset of accurate rotational spectra occurs experimentally, appears to be a significant success of the theory. The spectrum of ^{152}Sm is only roughly rotational, with the first 2^+ state at 121 keV, significant departures from the $I(I+1)$ rule, and states only identified through the 6^+ level, whereas ^{154}Sm is an excellent rotator with its first excited state at 82 keV and even the 8^+ energy accurately specified by $I(I+1)$. With internal evidence that the approximation of a single deformed intrinsic state is breaking down corroborated by experimental verification, it would be quite misleading to mock up the behavior of light rare earths by adjustment of the force parameters. It would appear much more fruitful to look at a suitably generalized theoretical description, such as the generator coordinate theory.

The case for the discrepancies in 4^+ and 6^+ transition densities is not as clear cut. From the discussion in Sec. II E, it is clear that the approximation that the range of $\exp(-\frac{1}{2}\beta^2\langle Jy^2\rangle)$ is small compared with that of the rest of the integral in Eq. (4) must break down for some high value of l. As yet, it is not clear whether such a discrepancy between a simple Legendre expansion and proper projection should be significant for $l \sim 6$, although preliminary estimates with deformed oscillator wave functions yield projection corrections for $0 \rightarrow 6$ form factors of the order of 10% and of the proper sign.[22] Even more complicated effects may be relevant, for such high multipoles may be sensitive to variation after, rather than before, projection, or even the projection of a pure angular momentum state out of a generator-coordinate wave function. At the very least, it appears that there are many legitimate limitations of the approximation by a single intrinsic state which must be investigated before it makes sense to try to improve the transition densities by modification of the effective interaction. Some indication as to whether the intrinsic state approximation or effective interaction is at fault will be afforded by the agreement for the 6^+ transition density in ^{238}U, since both the projection corrections, which vary as $1/\langle J_y^2\rangle$, and the corrections for collective motion will be much smaller than for the rare earths.

IV. CHARGE DENSITY DIFFERENCES IN THE NICKEL REGION

Measurement of charge density differences between neighboring isotopes specifies the static response of the proton distribution to the addition of neutrons. Differences between isotones yield a combination of the spatial distribution of the valence protons and the distortion of the core charge density. In combination, such data provide an exceedingly stringent test of any theory.

A. Polarization of spherical nuclei

For spherical nuclei, the mean-field approximation works quite well in describing valence proton wave functions and the polarization observed in isotope shifts. It is characteristic of spherical mean-field theories that the core is quite stiff and dilates only slightly in response to the enlargement of the single-particle potential produced by the addition of valence neutrons. Quantitatively, a scale of response may be set by that of a simple liquid drop, with radius $r \sim r_0 A^{1/3}$. Then the standard $A^{1/3}$ response would be $\Delta r/r = \frac{1}{3}\Delta A/A$. For spherical nuclei, one calculates and observes

isotope shifts ranging from 30% to 50% of the standard $A^{1/3}$ response.

Considerable success in describing tin isotopes has been obtained using DDHF theory with a realistic interaction.[23] Experimentally, tin charge radii increases are 54% of those expected from the $A^{1/3}$ law, i.e., $\Delta r/r = 0.54 \times \frac{1}{3}\Delta A/A$, and the prediction of Ref. 23 is 41%. The spherical mean-field analysis is expected to work reasonably well in tin because the proton shell closure at 50 keeps the nuclei spherical, and tends to inhibit the excitation of protons into normally unoccupied orbitals. Thus, the only possible response of the protons is a spherical dilation in the presence of the enlarged nuclear potential.

To verify that this physical picture is applicable to spherical nuclei throughout the Periodic Table, we have also compared the theoretical DDHF predictions for ^{204,206,208}Pb with experiment[19,24,25] in Table II. The first line shows the change in the charge radius due to the spherically symmetric polarization of the proton core, and corresponds to 43% and 47% of the $A^{1/3}$ law for the two isotope shifts, respectively. The second line includes as well the effect of the neutron charge factor,[26] which shifts the radius by $l\mu_N/2m^2rZ = -0.0419l/rZ$ for each neutron in a $j = l + \frac{1}{2}$ state and by $0.0419(l+1)/rZ$ for each neutron in a $j = l - \frac{1}{2}$ state. The electromagnetic effect of the $3p_{1/2}$ neutron in ^{208}Pb is rather negligible, but the $2f_{5/2}$ neutrons are somewhat more significant in the ^{204}Pb-^{208}Pb shift. If one repeats the calculation, removing the artificial constraint that ^{204}Pb and ^{206}Pb must remain spherical, the third line in Table II shows that the polarization increases slightly, although not dramatically, yielding reasonable agreement with experiment, especially if the spin-orbit shift from the second line is also added in. Thus, the physical picture of monopole dilation is essentially substantiated, and distortion effects play only a secondary role.

TABLE II. Theoretical and experimental values of Pb isotope shifts.

	Δr_c(208-206) (am)	Δr_c(208-204) (am)
Spherical, no spin-orbit	7.6	16.8
Spherical, with spin-orbit	7.9	17.9
Deformed, no spin-orbit	9.6	18.8
Expt. Ref. 19	11	21
Ref. 24	9 ± 0.5	18.6 ± 1.5
Ref. 25	13	24

B. Polarization of soft nuclei in the nickel region

In contrast, in the Fe, Ni, and Zn isotopes, one might expect the essential physics of polarization to be rather different. Since the Fe and Zn isotopes have open proton shells, the proton wave functions have much greater freedom to respond to the presence of additional valence neutrons than simply through the spherically symmetric dilation of the occupied proton wave functions described above. Even in the case of Ni, which is nominally a spherical closed shell for protons, we shall see that deformation effects may also play a significant role. A quantitative measure of how much polarization is omitted in the spherical approximation is obtained by calculating the spherically symmetric mean-field response to the addition of neutrons and seeing how much it underestimates the isotope shift. As the theory is extended to allow more and more general forms of proton response, the isotope shift should increase and approach the experimental value.

Whereas the wave functions of the present work are more general than a single spherically symmetric determinant, they are still subject to three essential limitations:

(1) As emphasized in connection with the rare earths, we consider only a single intrinsic state. If the energy of deformation curve is very soft, the sizable shape oscillations expected in the collective coordinate will require a more general generator-coordinate or multiconfigurational wave function.

(2) Only axially symmetric deformations are considered. In the case of ^{58}Fe, minima have been obtained for triaxially deformed configurations,[27] so some essential shape degrees of freedom may be omitted from the present calculation.

(3) The BCS wave function and pairing residual interaction, in addition to unrealistically averaging the state dependence of the $J=0$ $T=1$ matrix elements as discussed previously, are also overly restrictive. Only excitations corresponding to pairs of protons or neutrons are included, and the residual interaction between neutrons and protons, which should be particularly effective in polarizing the protons, is completely omitted.

Since, in general, the freezing of degrees of freedom or imposition of constraints on the form of wave function decreases its response to an external potential, we expect that the omission of more general forms of configuration admixture or shape deformation results in too small an isotope shift, whereas the errors associated with the oversimplified constant gap pairing approximation are clearly of undetermined sign.

The qualitative effects of deformation and pairing on the polarization of the Fe isotopes are shown in Fig. 6. The short dashed lines indicate

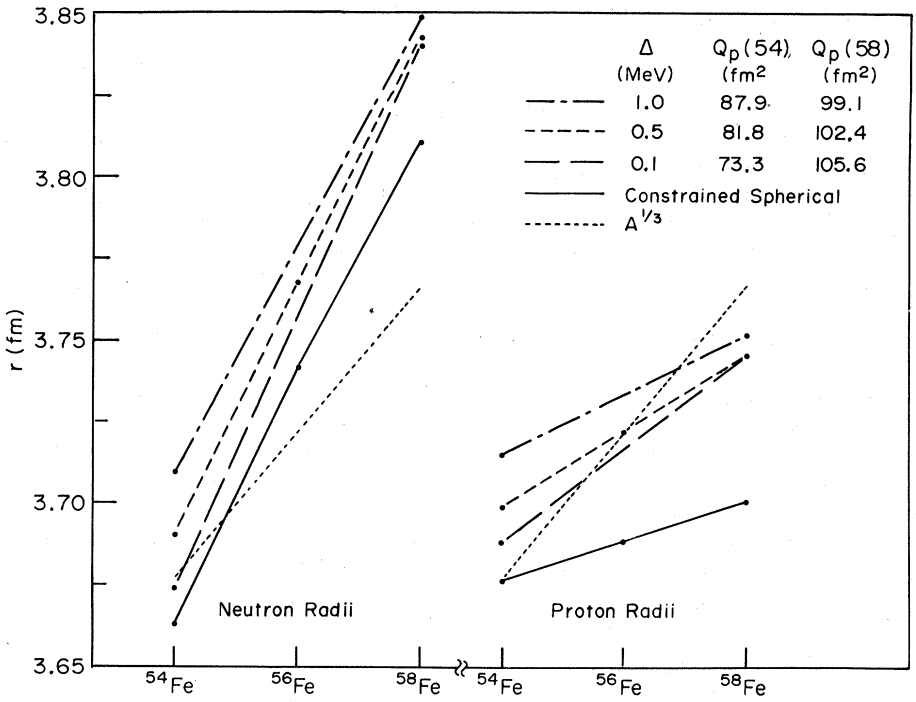

FIG. 6. rms radii for Fe isotopes obtained with alternative theories described in the text.

the standard $A^{1/3}$ radius change $\Delta r/r = \frac{1}{3}\Delta A/A$ expected for a simple liquid drop. Irrespective of the details of the theory, the addition of neutrons increases the neutron radius significantly more than the $A^{1/3}$ law. As noted previously, the response of spherically constrained protons (solid line) is roughly one-third of the $A^{1/3}$ value. With deformation and a very small pairing gap, $\Delta = 0.1$ MeV (long dashed lines), the polarization is significantly greater, reproducing almost two-thirds of the $A^{1/3}$ response as the addition of prolate orbitals outside the neutron shell closure at 28 significantly deforms the core. In the nickel region, mass differences indicate that the gap should be roughly 1.5 MeV, which is consistent with the matrix elements calculated in Ref. 13, and is the value used in all subsequent figures. One observes from Fig. 6 that increasing the pairing decreases the polarization. Experimentally,[7] the radii in Fe increase approximately as the $A^{1/3}$ law, so the introduction of deformation goes a long way toward resolving the glaring discrepancy between the spherically symmetric response and experiment.

C. Energy of deformation curves and qualitative behavior of radii

Figure 7 displays the energy of deformation vs mass quadrupole moment curves calculated for these isotopes. Note that, with the exception of ^{70}Zn which has a closed neutron shell, none of the minima are sufficiently deep and narrow to validate description by a single deformed intrinsic state. Thus, the most we may hope to extract from the present results is a qualitative impression of the spread and mean deformation of the collective wave function determined by the potentials in Fig. 7, and how these values would vary from nucleus to nucleus.

One check on these deformation curves is afforded by the extraction of a charge quadrupole moment of 100 fm^2 for ^{56}Fe from α scattering.[28] Although we make no claim that ^{56}Fe should be a pure rotator, the collective wave function should be peaked about a mass quadrupole moment of 200 fm^2, and the $B(E2)$ transition strength should therefore evidence collectivity characteristic of a charge quadrupole moment of 100 fm^2.

A second check of the systematics is provided by neutron occupation probabilities. Table III compares the theoretical occupation probabilities calculated with $\Delta = 1.5$ MeV and Q_0 constrained to be zero with those extracted from experiment.[29]

For very flat deformation curves, or those with an actual minimum at $Q_0 = 0$, we should expect qualitative agreement, with reasonable allowances for experimental uncertainties. For deformation curves with either prolate or oblate minima, substantial deviations are expected, especially in the $f_{5/2}$ occupation, because of the crossing of Nilsson

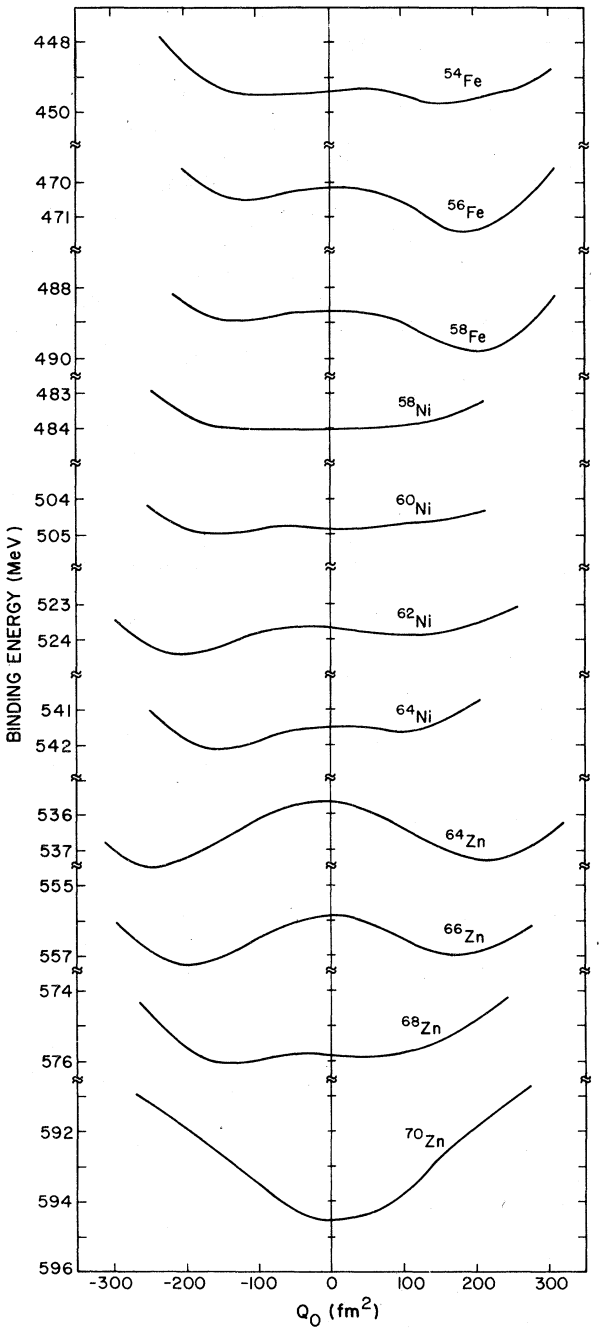

FIG. 7. Energy of deformation curves versus mass quadrupole moment for selected nuclei in the nickel region.

levels originating from the spherical $f_{5/2}$ orbitals. It is gratifying that the biggest $\Delta f_{5/2}$ discrepancy in Fe occurs for well deformed ^{58}Fe; that the $\Delta f_{5/2}$ discrepancies in the Ni isotopes are rather small, consistent with the rather flat deformation curves and closed proton shell; and that the biggest Zn discrepancies occur for ^{64}Zn and ^{66}Zn which have

TABLE III. Comparison between theoretical neutron occupation probabilities for constrained spherical calculations with $\Delta = 1.5$ MeV and the experimental values (given in parentheses) from Ref. 29. The quantity $\Delta f_{5/2}$ is the difference between the experimental and theoretical $1f_{5/2}$ occupation and provides a signature of substantial deformation.

Z	N	$2p_{3/2}$	$2p_{1/2}$	$1f_{5/2}$	$1g_{9/12}$	$\Delta f_{5/2}$
26	28	0.3	0.1	0.1	0.1	
		(0)	(0)	(0)	(0)	−0.1
26	30	1.6	0.2	0.3	0.1	
		(1.0)	(0.5)	(0.5)	(0)	0.2
26	32	3.0	0.4	0.5	0.1	
		(1.5)	(0.2)	(2.3)	(0)	1.8
28	30	1.5	0.2	0.3	0.1	
		(1.0)	(0.2)	(0.8)	(0)	0.5
28	32	2.9	0.4	0.6	0.1	
		(2.1)	(0.4)	(1.5)	(0)	0.9
28	34	3.5	0.8	1.5	0.1	
		(2.9)	(0.8)	(2.3)	(0)	0.8
28	36	3.7	1.2	2.8	0.2	
		(3.2)	(1.4)	(3.4)	(0)	0.6
30	34	3.5	0.7	1.6	0.2	
		(1.5)	(0.6)	(3.9)	(0)	2.3
30	36	3.7	1.1	2.9	0.2	
		(2.7)	(0.9)	(4.4)	(0)	1.5
30	38	3.8	1.5	4.4	0.3	
		(2.7)	(0.7)	(5.6)	(1.0)	1.2
30	40	3.9	1.8	5.5	0.5	
		(4.0)	(1.6)	(4.4)	(2.0)	−1.1

both prolate and oblate minima.

Figure 8 emphasizes the sensitivity of the rms charge radius to the quadrupole deformation. Thus, as the collective wave function becomes more and more concentrated at positive Q_0 as one progresses through the Fe isotopes, for example, the increase in charge radius may be appreciably greater than the indicated spherical increases. A very crude estimate of the range of radii which might be expected if one allowed for a collective wave function which sampled a reasonable range of deformations is presented in Fig. 9. The experimental radii[7] multiplied by $A^{-1/3}$ are denoted by the crosses, so that liquid drop behavior would yield a horizontal line. The bottoms of the theoretical error bars denote the rms radii at $Q_0 = 0$ from Fig. 8, which are the smallest radii one would obtain unless some complicated interference occurred in a collective or generator-coordinate wave function. The top of each error bar is defined to be the value of the charge radius at the most distant minimum of the deformation curve. Presumably a collective wave function will sample configurations with even larger radii, but no reasonable alternative prescription occurred to us. Thus, the error bars provide a

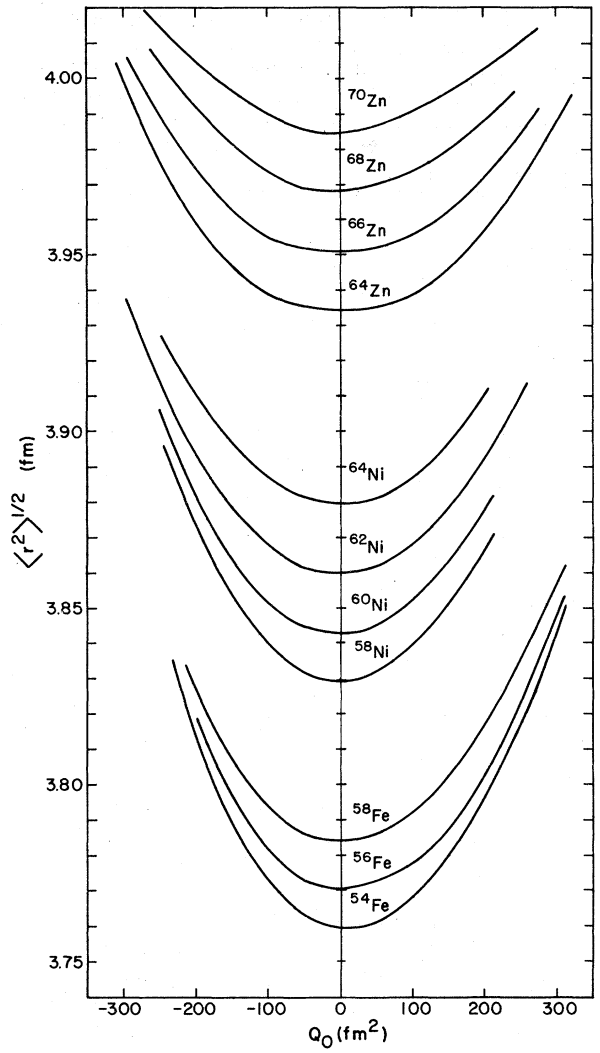

FIG. 8. rms charge radii as a function of mass quadrupole moment for the same calculation shown in Fig. 7.

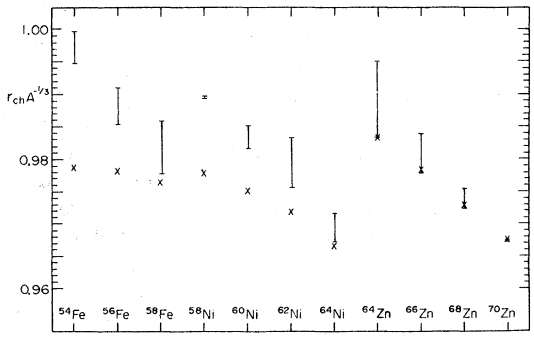

FIG. 9. Comparison of experimental values of $r_{ch}A^{-(1/3)}$, denoted by crosses, with theoretical estimates described in the text (solid error bars).

qualitative hint as to what range of radii might arise from more sophisticated calculations. In both the Fe and Ni isotopes, one observes that the trend from spherical to deformed shapes, i.e., from the bottom to the top of the error bars, agrees better with the systematic behavior than the purely spherical results. In the Zn isotopes, we regard it as fortuitous that the spherical calculations in all cases agree well with experiment. While it is possible that a two-sided minimum admixes more nearly spherical components than the one-sided minima in Fe and Ni, our preceding arguments favor radii in ^{64}Zn and ^{66}Zn which are definitely higher than experiment. The only nucleus in the entire calculation for which the approximation is manifestly valid is ^{70}Zr, and it is at least reassuring that this radius is accurately reproduced.

D. Charge density distributions

Recent elastic electron scattering experiments[8,30] have revealed certain fine details of the spatial charge distributions in the nickel region. Clearly, given the inadequacy of the theory discussed in the last section, one should not expect a quantitative theoretical explanation of all these details. However, several salient points have arisen which merit discussion.

Figure 10 displays charge density differences between neighboring nuclei which, in the pure shell model, would differ by the addition of two $1p_{3/2}$ neutrons and protons, respectively. The shaded areas represent the so-called model independent analyses of the experimental data[8] which are intended to bracket the true density distribution. The solid curves denote the isotope and isotone shifts obtained from the differences between spherical DDHF calculations for each nucleus. The ^{64}Zn-^{62}Ni isotone shift is dominated by the valence $1p_{3/2}$ proton wave function, and in the pure shell model one would expect an interior zero due to the radial node of the $1p_{3/2}$ state. The spherical calculation does not exactly reproduce this interior zero because of a slight polarization of the core, but the simple $1p_{3/2}$ structure is still quite evident. Although beyond 4 fm the spherical result is consistent with experiment, the distinct interior structure associated with the p state is in qualitative disagreement. Hence, it is instructive to see how different the density difference appears if one considers deformed intrinsic states. Since Fig. 7 indicates that both ^{64}Zn and ^{62}Ni have oblate minima, the difference between the two oblate solutions in the minima is shown by the dashed line in Fig. 10. The essential point is that virtually all of the interior structure is washed

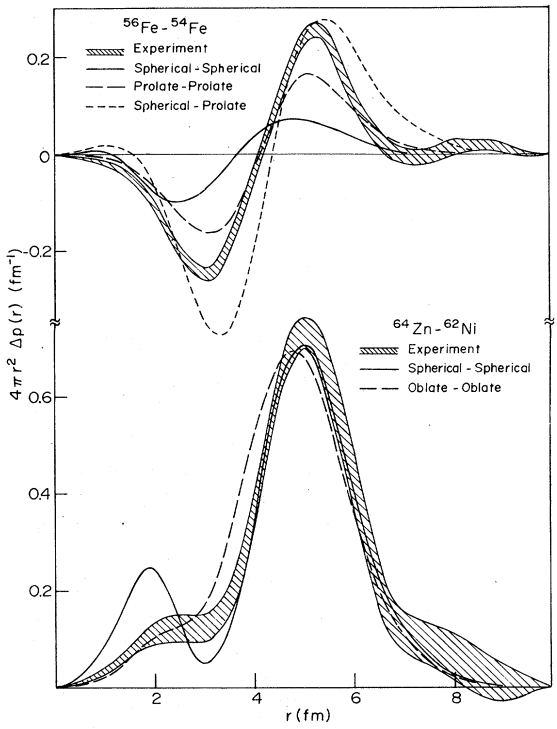

FIG. 10. Results of the experimental analysis of isotope and isotone differences in Ref. 8, shaded areas, with alternative calculations described in the text.

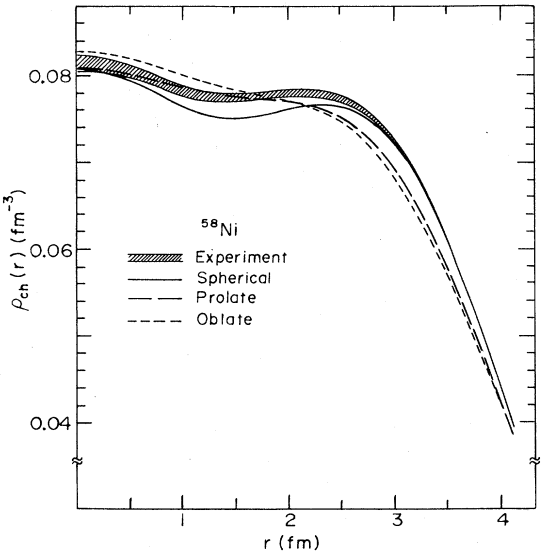

FIG. 11. Comparison of the experimental determination of the ^{58}Ni charge density of Ref. 19, shaded area, with three calculations described in the text. Note the expanded density scale does not go to zero.

out in this case. In an actual calculation in which the wave function is expressed as a superposition of various deformations, it appears quite plausible that the final result would indeed have much less structure than the spherical result.

The ^{56}Fe-^{54}Fe isotone difference between two spherical solutions, indicated by the solid lines in the top of Fig. 10, is much smaller than experiment, consistent with the fact that the spherical solution radius shift is only about one-third of that measured experimentally. Taking the difference between the two solutions at the respective prolate minima does much better (long dashes), and the extreme case of comparing spherical ^{54}Fe with prolate deformed ^{56}Fe significantly overestimates the observed polarization. Hence, there is again hope that a superposition of solutions of various deformations will come much closer to experiment than the results with a single intrinsic state.

The interior density distribution obtained from high momentum transfer elastic electron scattering from ^{58}Ni is shown by the shaded area in Fig. 11 on an expanded density scale.[30] It has been emphasized that the observed interior oscillations are significantly smaller than those predicted by various spherical HF calculations.[31] As claimed, the interior charge density for our spherical solution, denoted by the solid line in Fig. 11, evidences more structure than seen experimentally. Furthermore, as explained in Ref. 1, retention of a finite range direct force instead of using the DME functional will increase, not decrease, the discrepancy.

Hence, we have also displayed by the long and short dashed lines in Fig. 11, the ρ_0 components of the prolate and oblate charge densities at the extreme ends of the energy plateau of Fig. 7. Here again, the salient point is the degree to which deformation, either prolate or oblate, washes out the pronounced spherical shell structure. If one considers a superposition of states of varying deformation, it appears quite plausible that the composite effect of the nearly spherical and well-deformed components will yield diminished shell structure comparable to that observed experimentally.

V. SUMMARY

From the preceding results, it is evident that the mean-field description of well-deformed rotational nuclei using a realistic effective interaction is extremely successful. Energies, radii, and elastic electron scattering cross sections are given just as well as in spherical nuclei, and $B(E2)$ transition strengths and $0^+ \rightarrow 2^+$ inelastic electron scattering form factors are well reproduced. Only for high multipole transitions does one begin to encounter significant discrepancies in such nuclei.

For nuclei which do not have well-defined minima

TABLE IV. Convergence of ^{56}Ni binding energy and charge radii as a function of basis size N_0 and number of integration points K.

I	$N_0=14$, $K=I$		$K=16$, $N_0=I$	
	BE (MeV)	r_p (fm)	BE (MeV)	r_p (fm)
8			442.23	3.721
10	443.86	3.732	442.89	3.726
12	443.19	3.728	443.40	3.730
14	443.48	3.729	443.46	3.729
16	443.46	3.729	443.51	3.730
"Exact"			(443.34)	(3.732)

and do not exhibit rotational spectra, whereas the present description may yield valuable qualitative insights, it is not sufficient to provide quantitative precision. At the least, however, the theory does appear to provide a criterion which accurately diagnoses its validity, insofar as the energy of deformation curves have been completely reliable indicators of its accuracy in every case we have examined.

The obvious extension for future work will be to superpose families of determinants of different deformations via the generator-coordinate method. Although such a calculation in an harmonic-oscillator basis of the size required to attain adequate convergences in this present work appears to us quite cumbersome, work in progress using deformed determinantal wave functions in coordinate space[32] suggests feasibility through the rare-earth region.

ACKNOWLEDGMENTS

It is a pleasure to acknowledge fruitful discussions with W. Bertozzi, G. Fricke, J. Heisenberg, S. Kowalski, E. B. Shera, and H. D. Wohlfahrt, whose beautiful experiments provided the primary impetus for this work, and who provided experimental data prior to publication. In addition, the authors are grateful to A. Zarringalam for providing his preliminary results on angular momentum projected transition densities. The numerical calculations were carried out at the LASL Central Computing Facility with the financial support of the LASL Physics, Theoretical, and Computing Divisions.

TABLE V. Convergence of ^{238}U binding energy and charge radius as a function of N_0 and K.

N_0	K	BE (MeV)	r_p (fm)	Q_0 (fm^2)
12	14	1797.89	5.8003	2752
14	16	1800.30	5.7994	2741

APPENDIX A: NUMERICAL CONVERGENCE

The convergence in the basis size N_0 and the number of numerical quadrature points K was explored numerically for ^{56}Ni, which is spherical and thus comparable to the "exact" solution of Ref. 15. Table IV shows the changes in binding energy and proton radius as N_0 and K are separately varied. Note that whereas the binding energy increases monotonically in N_0 since fixed K yields a variational principle, increasing K may decrease, as well as increase, binding. The small discrepancy between the 16,16 result and the "exact" spherical calculation was not resolved and, in any event, is insignificant physically. All of the calculations in the nickel region were performed with $N_0=10$ and $K=12$, which made it unnecessary to optimize the oscillation basis parameters.

Convergence for ^{238}U is indicated in Table V. Since optimizing the basis to minimize the energy yields no particular advantage for the convergence of the one-body density, the basis has not been optimized. Presumably, the convergence for the rare earths is much better so all rare-earth results were computed with $N_0=12$ and $K=14$. The energy of deformation curves for the actinides in Fig. 1 was also calculated with $N_0=12$ and $K=14$, but the final solutions at the minima used $N_0=14$, $K=16$. Although the convergence of $\rho_l(r)$ degrades with increasing l, the change in $\rho_6(r)$ in ^{238}U upon increasing N_0 from 12 to 14 and K from 14 to 16 was roughly of the order of 5% in the interior and surface, rendering it unlikely that nonconvergence accounts for the 6^+ discrepancies. Computing time was roughly proportional to $N_0^{3.5}K^2$.

*Work supported by the Energy Research and Development Administration under Contracts Nos. EY-76-C-02-3069.*000 and W=7405-ENG. 36.

†Alfred P. Sloan Foundation Research Fellow.

‡Present address: Institut für Kernphysik, D-5170 Julich, Germany.

[1]J. W. Negele, in Proceedings of the Conference on Diffusion d'electrons a Energie Intermediaire, Saclay, 1976, edited by J. B. Bellicard *et al.* (unpublished), p. 241.

[2]J. G. Zabolitzky, Nucl. Phys. A228, 272 (1974); A228, 285 (1974) and references therein.

[3]J. G. Zabolitzky, Phys. Rev. C 14, 1207 (1976).

[4]J. L. Friar and J. W. Negele, in *Advances in Nuclear Physics*, edited by M. Baranger and E. Vogt (Plenum, New York, 1975), Vol. 8.

[5]T. Cooper, W. Bertozzi, J. Heisenberg, S. Kowalski,

W. Turchinetz, C. Williamson, L. Cardman, S. Fivorinsky, J. Lightbody, Jr., and S. Penner, Phys. Rev. C 13, 1083 (1976).
[6]W. Bertozzi, C. Creswell, J. Heisenberg, A. Hirsch, M. Hynes, S. Kowalski, C. P. Sargent, and W. Turchinetz (unpublished).
[7]E. B. Shera, E. T. Ritter, R. B. Perkins, G. A. Rinker, L. K. Wagner, H. D. Wohlfahrt, G. Fricke, and R. M. Steffen, Phys. Rev. C 14, 731 (1976).
[8]R. Neuhausen, in Proceedings of the Conference on Diffusion d'electrons a Energie Intermediaire, Saclay, 1976 (see Ref. 1), p. 315.
[9]H. Flocard, P. Quentin, A. K. Kerman, and D. Vautherin, Nucl. Phys. A203, 433 (1973).
[10]D. Vautherin, Phys. Rev. C 7, 296 (1973).
[11]J. W. Negele and D. Vautherin, Phys. Rev. C 5, 1472 (1972). Note that in Table I, the coefficient D_{03} should be $-6.626\,99\times 10^{5}$ instead of the misprinted value $-6.626\,99\times 10^{3}$.
[12]M. Brack (private communication).
[13]J. W. Negele, Nucl. Phys. A142, 225 (1970).
[14]F. Villars and N. Schmeing-Rogerson, Ann. Phys. (N.Y.) 63, 443 (1971).
[15]J. W. Negele and D. Vautherin, Phys. Rev. C 11, 1031 (1975).
[16]H. Flocard, P. Quentin, and D. Vautherin, Phys. Lett. 46B, 304 (1973).
[17]J. Decharge, M. Girod, and D. Gogny, Phys. Lett. 55B, 361 (1975).
[18]C. W. deJager, H. deVries, and C. deVries, At. Data Nucl. Data Tables 14, 479 (1974).
[19]R. Engfer, H. Schneuwly, J. L. Vuilleumier, H. K. Walter, and A. Zehnder, At. Data Nucl. Data Tables 14, 509 (1974).
[20]K. E. G. Löbner, M. Vetter, and V. Hönig, Nucl. Data A7, 495 (1970).
[21]G. Scharff-Goldhaber (private communication).
[22]A. Zarringalam (private communication).
[23]X. Campi, D. W. L. Sprung, and J. Martorell, Nucl. Phys. A223, 541 (1974).
[24]P. L. Lee and F. Boehm, Phys. Rev. C 8, 819 (1973).
[25]D. Kessler, H. Mes, A. C. Thompson, H. L. Anderson, M. S. Dixit, C. K. Hargrove, and R. J. McKee, Phys. Rev. C 11, 1719 (1975); K. W. Ford and G. A. Rinker, Jr., *ibid.* 7, 1206 (1973); 9, 2444 (1974).
[26]W. Bertozzi, J. Friar, J. Heisenberg, and J. W. Negele, Phys. Lett. 41B, 408 (1972).
[27]S. E. Larssen, G. Leander, I. Ragnarssen, and G. Alenius, Nucl. Phys. (to be published).
[28]H. J. Gils, H. Rebel, G. Nowicki, D. Hartmann, A. Ciocanel, H. Klewe-Nebenius, and K. Wisshak, Karlsruhe report, 1974 (unpublished).
[29]R. Sherr (private communication).
[30]I. Sick, J. B. Bellicard, M. Bernheim, B. Frois, M. Huet, Ph. Leconte, J. Mougey, Phan Xuan-Ho, D. Royer, and S. Turck, Phys. Rev. Lett. 35, 910 (1975).
[31]I. Sick, in *High-Energy Physics and Nuclear Structure—1975,* edited by D. E. Nagle *et al.* (American Institute of Physics, New York, 1975), p. 388.
[32]J. W. Negele, Proceedings of the Conference on Gross Properties of Nuclei and Nuclear Excitations, Techniche Hoschschule Darmstadt report, 1976 (unpublished), p. 36; P. Hoodbhoy and J. W. Negele (unpublished).